KRONOS FUSION ENERGY

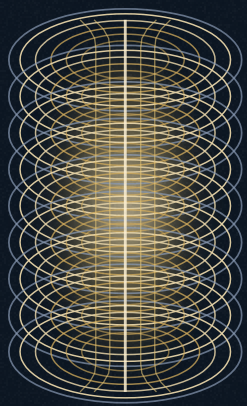

PAPER 2.19 · THE KRONOS 2026 SERIES

Fused Strain-Rate and Magnetization Quench Detection with In-Winding NV-Diamond Sensing for No-Insulation REBCO Breeder Magnets

The unsolved protection problem of high-temperature-superconductor (HTS) fusion magnets is that no-insulation (NI) REBCO windings quench too slowly for terminal-voltage detection...

Read it live — 3-D model · physics validator · film series

BY P I FORD, R J WEGGEL AND C WEGGEL

2026 · EDITORIAL EDITION

THE OFFICIAL RECORD

What this document is, and how to read its numbers

This is a combined editorial. It gathers, in one volume, the two design studies Kronos Fusion Energy released in 2026 — a compact spherical-tokamak tritium/helium-3 breeder and a deuterium–helium-3 tandem-mirror generator — together with the intellectual-property estate, the people, and, in the internal edition, the full commercial case. The scientific text is the same text that appears in the arXiv preprints and the journal submissions; the editorial adds the apparatus a reader needs to hold the whole program at once, and nothing in the physics is altered to fit it.

THE HONESTY STANCE IS THE ASSET

Every headline quantity carries an **evidence class** — DERIVED RECOMPUTED MEASURED REQUIREMENT — and, where a number is a modelled extrapolation rather than a demonstrated value, it is labelled as such and its downside is shown next to it. Several quantities in the underlying corpus moved after first publication; where a value has been withdrawn or restated, the record says so plainly. This is deliberate: a diligence team will find the load-bearing assumptions, so the document surfaces them first.

TWO EDITIONS

This volume is issued in two editions. The **public edition** (light) carries the physics and the design only — no dollar, price, or per-kilogram figure appears anywhere in it. The **internal edition** (dark) adds the economics, the funding architecture, and the defense-commercial analysis, and is marked *Confidential* accordingly; it is not for public distribution. Where the commercial case rests on a modelled assumption rather than a demonstrated one, it is labelled as such and its downside is shown alongside it, on the same terms as the physics.

TITLE	The Kronos Fleet — Hyperion · Aegis · MetroVolt: A Combined Design & Commercialization Study
AUTHOR	Priyanca Ford, Founder & CEO, on behalf of Kronos Fusion Energy
EDITION	2026 Combined Editorial · first issue
COMPANION WORKS	The five-paper arXiv drop — (1) Breeder, (2) Burner, (3) REBCO magnet & tape, (4) Direct Energy Conversion, (5) AI/ML/Quantum control — with matching numbered Zenodo deposits, plus the IOP journal and IAEA-FEC submissions. Patents were filed before the drop.
NAMING	Hyperion = the breeder; Aegis (defense) and MetroVolt (data-center) = one generator in two housings. Internal mode letters (D1, L) do not appear on public surfaces.
STATUS	Conceptual design & simulation study. Nothing herein is a construction commitment.

HOW TO READ THIS VOLUME

The fleet at a glance, and the way its numbers are marked

This volume opens with *Orientation*, presents the five research papers as a bound sequence, and closes with the *Apparatus*. *Foundations* sets out the three general results both machines rest on. *Paper One* is the Hyperion breeder; *Paper Two* the Aegis / MetroVolt generator; *Papers Three, Four and Five* are the enabling science — high-field REBCO magnets and tape, direct energy conversion, and the AI / ML / quantum control stack. A *Digital Twin & 3-D Model* part follows, then the *Environmental* profile. The *Economics* and levelized cost and the *Business Case* and diligence record appear in the internal edition only; the *Simulations* proof record and the Apparatus — patent portfolio, team, limitations, and sources — close both editions.

THE FLEET AT A GLANCE

	HYPERION	AEGIS	METROVOLT
Role	Strategic-isotope foundry	Defense installation power	Campus power
Machine	**Spherical tokamak**	**Tandem mirror**	**Tandem mirror**
Fuel	Deuterium–tritium	Deuterium–helium-3	Deuterium–helium-3
Delivers	Tritium · ^{3}He · 14 MeV n	Resilient installation power	Firm campus power
Physics bar	**Fusion gain only**	Closure (gates named)	Closure + lunar ^{3}He
In the fleet	Breeds the fuel	Proves the generator	Commercial destination

HOW THE NUMBERS ARE MARKED

Every headline quantity carries an evidence class — DERIVED from first principles, RECOMPUTED from raw data, MEASURED in hardware, or a REQUIREMENT yet to be met. Financial figures carry a case label and are confined to the internal (confidential) edition. Values that moved after first publication are shown as withdrawn or restated rather than quietly changed. A capability you can evaluate is one whose limits are on the page.

ABSTRACT

Fused Strain-Rate and Magnetization Quench Detection with In-Winding NV-Diamond Sensing for No-Insulation REBCO Breeder Magnets

The unsolved protection problem of high-temperature-superconductor (HTS) fusion magnets is that no-insulation (NI) REBCO windings quench too slowly for terminal-voltage detection to act before the local hot spot reaches a damaging temperature: the normal zone propagates at millimetres per second, so the resistive voltage integrated along it stays small while the deposited energy density climbs. We formalise and evaluate a fused-detector scheme that does not wait for voltage. Two prompt, physically independent precursors are read inside the winding pack — the mechanical *strain-rate* transient as the normal zone thermally expands ($\dot{\varepsilon} \sim 1.3 \times 10^{-3}\,\mathrm{s}^{-1}$), and the local *magnetization* change as the screening current redistributes out of the quenched turn ($\Delta B \sim 8.5\,\mu T$ over the detection window). Each is reduced to a matched-filter window statistic; because the two modalities fail in uncorrelated ways their quadrature fusion $z_F = (z_S + z_M)/\sqrt{2}$ carries a statistic whose detectability exceeds either channel. On a frozen 2×10^4-trial synthetic study in a deliberately hard, weak-fault regime the fused detector reaches an area under the receiver-operating characteristic (ROC) of $\mathbf{0.992}$ — against $\mathbf{0.976}$ for magnetization and $\mathbf{0.921}$ for strain alone — and a true-positive rate of $\mathbf{0.857}$ at the $\mathbf{1\%}$ false-positive rate a protection trip demands, versus $\mathbf{0.671}$ and $\mathbf{0.372}$ for the single channels. The magnetization channel is supplied by an in-winding ensemble nitrogen-vacancy (NV) diamond magnetometer with a shot-noise-limited sensitivity of $\mathbf{0.189}$ $\mathbf{pT\,Hz^{-1/2}}$ at $\mathbf{125}$ Hertz *bandwidth, resolvingtheconductor − scalequenchfieldstepataper − shotsignal − to − noiseratiooforder*10^9 ;*thesameNVensemblereadsfield(Zeeman)andstrain(zero − field − splitting)inonefrontend.Trippingtensofmillisecondsearliermovestheadiabatichot − spottemperaturebackunderitslimitthroughthecurrent − time(MIITs)integral.Theoneopenengineeringitem − − − theNVsensor′sneutrontolerance − − − isboundedbyamodel − fusionbackupthatretainsprecursorAUC*
\ge0.95*withtheNVchanneldegradedbyupto*39×
.*Everyheadlinequantityisafrozenanchorinthe Kronosphysicsde − riskingregister.Thisisaprotectionarchitectureatthemodel − and − benchstage, statedassuch; itseparatesthebreedercentrepost*(
16.84 T)*andtheburnerplug*(26.49 T$) as the two distinct magnets they are.

Open-access deposit (code & data, CC BY 4.0): DOI 10.5281/zenodo.22645752 · Zenodo community *kronos_fusion_energy*. Explore it live: interactive 3-D model · physics validator.

Keywords: REBCO quench detection sensor fusion NV-diamond magnetometry no-insulation magnet MIITs magnet protection

CONTENTS

Table of Contents

NOMENCLATURE

Symbols, units, and the names of things

Q	plasma (fusion) gain, P_{fus}/P_{aux}
Q_E	engineering gain, net electric out / recirculating in
H_{98}	confinement enhancement over the IPB98(y,2) scaling
Z_{eff}	effective ion charge
c_{ee}	electron–electron bremsstrahlung leading coefficient, 2.120022 (exact)
τ_E	energy confinement time
I_p	plasma current
R_0, a	major radius, minor radius
κ, δ	elongation, triangularity
β_N	normalized plasma beta (Troyon-normalized)
TBR	tritium breeding ratio
DEC	direct energy conversion
CF	plant capacity factor (availability)
FOAK / NOAK / BOAK	first / nth / best of a kind
Hyperion	the ST breeder (internal: Mode D2)
Aegis	the generator, defense/installation housing (internal: Mode M)
MetroVolt	the generator, data-center housing (Mode M)

§ 1

Introduction

THE SLOW-PROPAGATION PROTECTION PROBLEM

The compact, high-field spherical tokamak (ST) that makes an attractive neutron source and breeder platform is built around a high-temperature-superconductor magnet [1,2,3]. The Kronos Hyperion breeder holds a plasma current of $I_p = 9.66\,MA$ at a major radius of only $R_0 = 1.20\,m$ behind a centrepost magnet whose peak field is $16.84\,T$, delivering fusion power $P_{\text{fus}} = 85.04\,MW$ at gain $Q = 3.076$ in a negative-triangularity ($\delta = -0.30$) regime [30]. The magnets are wound from no-insulation (NI) REBCO coated conductor [4,6], the technology behind recent record fields [5]. NI winding self-protects against local defects by shunting current turn-to-turn, and it carries a large temperature margin — but the same properties make active protection hard. The normal-zone propagation velocity (NZPV) of NI REBCO is of order millimetres per second, two to three orders below the metre-per-second propagation of low-temperature superconductors. A developing hot spot can therefore reach a damaging temperature before the resistive voltage integrated over the slowly spreading zone rises above the inductive and noise background. Marchevsky's review states the consequence precisely: in HTS conductors the large margin and slow propagation mean voltage detection alone is inadequate, and the field must turn to non-voltage observables [7].

The protection question is therefore not “how do we measure the resistive voltage faster” but “what changes *early*”. Two observables do. When a REBCO turn goes normal the local temperature rises and the conductor expands, producing a prompt *strain-rate* transient; and the screening current that magnetizes the NI turn collapses as current redistributes, producing a prompt local *magnetization* change. Both precede the terminal voltage. This paper makes them the front end of protection.

PRIOR ART

The community response to slow-NZPV HTS protection has been a search for non-voltage observables. Salazar *et al.* demonstrated fibre-Bragg-grating (FBG) and ultra-long-FBG thermometry on VIPER cable at the SULTAN facility, reporting quench-like-event signal-to-noise ratios of 4–32 with response times from effectively instantaneous to a few seconds [8]. Teyber *et al.* showed that current-distribution monitoring detects both quench and mechanical damage in superconducting fusion cables [9]. Acoustic, co-wound, and Rogowski approaches have all been explored, and each reads one physical channel. In parallel, quantum magnetometry with nitrogen-vacancy (NV) centres in diamond has matured into a broadband, vector, chip-scale field sensor with a well-characterised shot-noise scaling [10,11,12]; NV ensembles are attractive precisely because they are solid-state, operate from cryogenic to elevated temperature, and read both field and strain through the ground-state spin Hamiltonian. What has not been assembled is a *fused* detector that combines two uncorrelated prompt precursors — one mechanical, one magnetic — into a single early-warning statistic, with the magnetic channel read locally, inside the winding, by an NV ensemble, and with the whole scheme evaluated in the low-signal regime that the slow-NZPV physics actually forces on a fusion magnet.

CONTRIBUTION

This paper contributes that detector and its analysis. We (i) write the governing model — the adiabatic hot-spot (MIITs) limit, the NI NZPV, and the two precursor physics — as explicit equations (§2); (ii) derive the matched-filter window statistics and their quadrature fusion, and the closed-form ROC of the resulting Gaussian detection problem (§2); (iii) give the shot-noise sensitivity and dual-mode (field +strain) readout of the in-winding NV ensemble, and the field step it must resolve (§2); (iv) specify the GPU-accelerated Monte-Carlo synthesis, the FEA-grounded coil critical-surface load-line, and the neutronics that produced the frozen numbers (§3); (v) report the detection performance, the sensor margin, the MIITs lead, the two-magnet margin map, and the neutron-degradation retention as figures and tables (§4); and (vi) benchmark the result quantitatively against the published quench-detection and quantum-sensing literature (§5). The detector is the reduced-to-practice magnet-protection subsystem of the Kronos four-twin control architecture [31]; it draws on the consumable-centrepost coil-integrity and fused-quench-detection case [32], the REBCO conductor and stabilizer materials basis [33], the first-principles radiation tolerance of centrepost REBCO [34], the engineering of the distinct $26.49\,T$ plug coil [35], the graph-neural-network state reconstructor that serves as the model-fusion backup channel [36], and the entanglement-enhanced magnetometry roadmap [37]. Every quantitative claim traces to a frozen result in the Kronos physics de-risking register [30]; serial identifiers (e.g. KX-L1-A20) are given inline so each number is auditable.

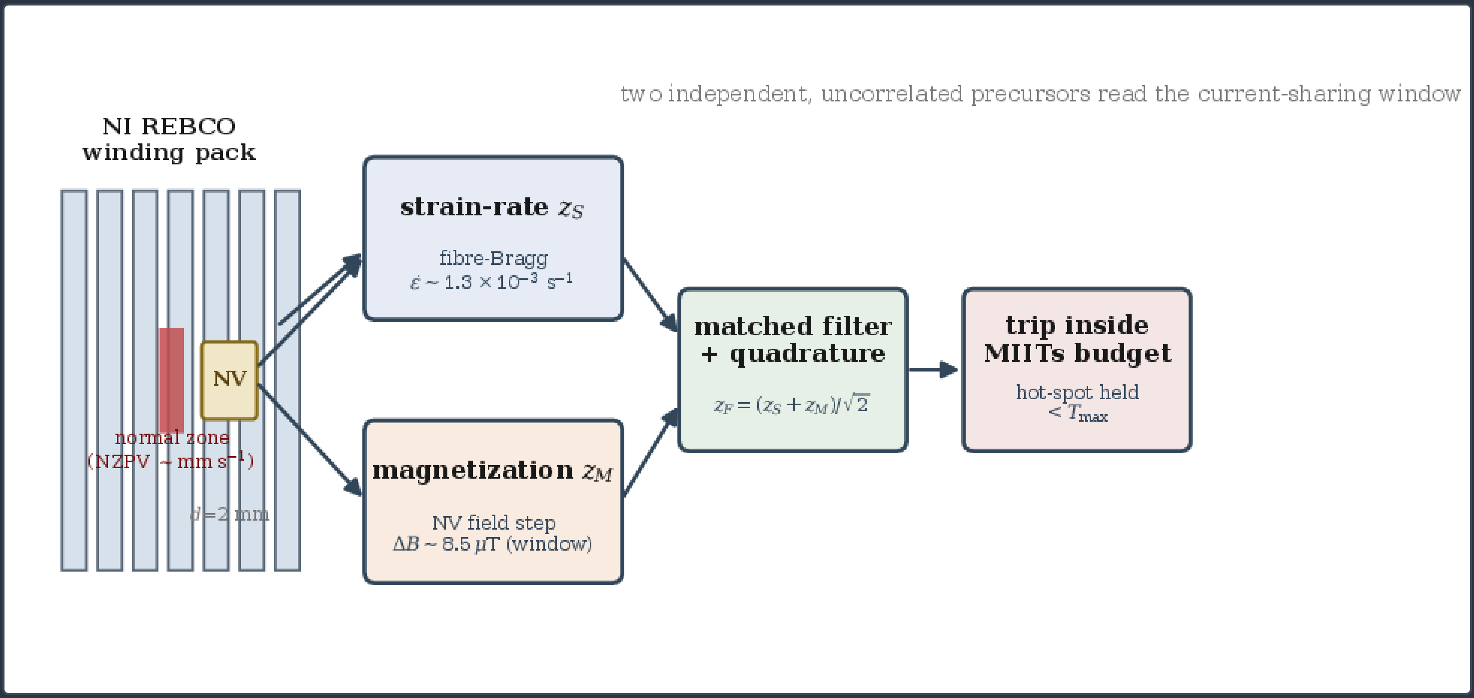

(Schematic.) The fused-detection front end inside the NI REBCO winding pack. A slowly propagating normal zone (NZPV $\sim$mm s^{-1}) drives two prompt, uncorrelated precursors: a fibre-Bragg strain-rate channel z_S and a magnetization channel z_M read locally by an in-winding NV ensemble at a $2\,mm$ standoff. Matched-filter window statistics are fused in quadrature (equation 7) and the detector trips inside the adiabatic hot-spot (MIITs) budget of equation (1). Structure only; no data values are drawn.

§ 2

Governing equations and formal problem

THE ADIABATIC HOT-SPOT LIMIT

Protection must act before the peak conductor temperature exceeds a material limit $T_{\max}$. Once a zone is fully normal the deposited energy is, to a good approximation, adiabatic on the millisecond-to-second timescale of interest, so the local energy balance $\rho_m c_p(T)\,\dot{T} = \rho_e(T)\,J^2$ integrates to the classical hot-spot ("MIITs") condition

$$\int_0^{t_d} J(t)^2\,\mathrm{d}t \;=\; \int_{T_0}^{T_{\max}} \frac{\rho_m\,c_p(T)}{\rho_e(T)}\,\mathrm{d}T \;\equiv\; \Gamma(T_{\max}),$$

where J is the current density in the stabilizer, $\rho_m c_p$ the volumetric heat capacity, ρ_e the resistivity, T_0 the operating temperature and t_d the total detection-plus-dump delay. The right-hand material function $\Gamma(T_{\max})$ is fixed by the conductor; the left-hand action integral, conventionally quoted in $\mathrm{MA}^2\,\mathrm{s}$ ("MIITs"), is what the winding must be held under. Equation (1) makes the protection requirement quantitative: for a given post-detection current waveform the peak temperature is a monotone function of t_d, so *every millisecond of earlier detection buys margin against* $T_{\max}$. The design intent is to keep the fused-detection hot spot well inside the conductor limit; the lead time the fused detector provides is the lever on t_d (§4).

SLOW NORMAL-ZONE PROPAGATION

The reason voltage detection is late is the smallness of the normal zone. In the one-dimensional adiabatic approximation the normal-zone propagation velocity along the conductor is

$$v_{\mathrm{NZP}} \;=\; \frac{J}{\rho_m c_p}\sqrt{\frac{\rho_e\,k}{T_t - T_0}}\,, \qquad T_t \;=\; \tfrac{1}{2}(T_{\mathrm{cs}} + T_c),$$

with k the axial thermal conductivity and T_t the transition temperature between the current-sharing temperature T_{cs} and the critical temperature T_c. For NI REBCO the large heat capacity and margin at $20\,K$-class operation push v_{NZP} to the order of millimetres per second. The resistive voltage $V \sim \rho_e J\,\ell_{\mathrm{nz}}$ scales with the normal length $\ell_{\mathrm{nz}} \sim v_{\mathrm{NZP}}\,t$, so a voltage threshold of a few millivolts is not crossed until the zone has grown — by which time the accumulated MIITs of equation (1) may already be large. A detector keyed to ℓ_{nz} is intrinsically late; a detector keyed to the *local* precursors below is not.

THE STRAIN-RATE PRECURSOR

Inside the normal zone the same Joule term drives a temperature rate

$$\dot{T} \;=\; \frac{\rho_e(T)\,J^2}{\rho_m\,c_p(T)},$$

and the conductor responds thermoelastically. The prompt observable is the thermal strain rate

$$\dot{\varepsilon}_{\mathrm{th}} \;=\; \alpha(T)\,\dot{T} \;=\; \frac{\alpha(T)\,\rho_e(T)\,J^2}{\rho_m\,c_p(T)},$$

with α the coefficient of thermal expansion. Equation (4) evaluated at the operating point gives a representative window-scale strain-rate transient $\dot{\varepsilon}_{\mathrm{th}} \sim 1.3 \times 10^{-3}\,\mathrm{s}^{-1}$ (register item; KX-L1-A20), well above the mechanical background of a steady magnet and resolvable by a co-wound fibre-Bragg grating. Because $\dot{\varepsilon}_{\mathrm{th}}$ responds to the local temperature rate rather than to the normal length, it leads the terminal voltage.

THE MAGNETIZATION / SCREENING-CURRENT PRECURSOR

An NI turn carries azimuthal screening (magnetization) currents that shield field changes; they store a local magnetic moment. When the turn quenches, transport current redistributes turn-to-turn through the characteristic contact time $\tau_{\text{ct}} = L_{\text{turn}}/R_{\text{ct}}$, and the screening current collapses. The collapse changes the local field at a sensor placed a standoff d from the conductor. For a turn carrying transport current I_{turn} the field scale at the sensor is

$$\Delta B \;=\; \frac{\mu_0\, I_{\text{turn}}}{2\pi d}\,,$$

which for a full-turn shed ($I_{\text{turn}} = 1\,kA$, $d = 2\,mm$) is $\Delta B \approx 100\,mT$. The screening-current *decay* signal integrated over the detection window is far smaller, of order $\Delta B \sim 8.5\,\mu T$ (register item; KX-L1-A20); it is this window-scale magnetization-decay perturbation that the detector reads, while the $100\,mT$ full-shed step sets the single-shot sensor margin (§2.7). The magnetization precursor is prompt for the same reason the strain-rate precursor is: it is set by the local current redistribution, not by the normal length.

MATCHED-FILTER WINDOW STATISTICS AND QUADRATURE FUSION

Let each channel deliver, over a detection window of N samples at rate f_s, a discrete signal $y = \mu\ \ h +\ \ n$, where h is the (unit-norm) precursor template, μ the amplitude, and n zero-mean noise of per-sample variance σ^2. The matched filter is the linear statistic that maximises detectability; its normalised output is

$$z \;=\; \frac{h^{\top}\quad y}{\sigma\,\|\quad h\|}\,, \qquad z \sim \begin{cases} \mathcal{N}(0,1) & \text{no quench (null)} \\ \mathcal{N}(\mu_z,1) & \text{quench (fault)}, \end{cases} \qquad \mu_z \;=\; \text{SNR}_{\text{sample}}\sqrt{N},$$

so the per-window detectability grows as $\sqrt{N}$ (the matched-filter gain). Two channels — strain-rate (z_S) and magnetization (z_M) — observe the same current-sharing window through uncorrelated noise. Their equal-weight quadrature fusion,

$$z_F \;=\; \frac{z_S + z_M}{\sqrt{2}}\,,$$

has unit variance under the null (so its false-alarm calibration is unchanged) and fault mean $\mu_{z_F} = (\mu_{z_S} + \mu_{z_M})/\sqrt{2}$; equivalently, for the optimally combined statistic the fused window SNR adds the single-channel ratios in quadrature, $\text{SNR}_F^2 = \text{SNR}_S^2 + \text{SNR}_M^2$. At the frozen operating point the window statistics are $\mu_{z_S} = 2.00$, $\mu_{z_M} = 2.78$ and $\mu_{z_F} = 3.38$ (KX-L1-A20); the geometry of equation (7) is drawn in figure 4.

CLOSED-FORM ROC OF THE GAUSSIAN DETECTOR

Because the fused statistic is Gaussian with a shifted mean, its receiver-operating characteristic is closed form. At a false-positive rate α the trip threshold is $z_\alpha = \Phi^{-1}(1-\alpha)$, and the true-positive rate and the area under the ROC are

$$\text{TPR}(\alpha) \;=\; \Phi\big(\mu_z - \Phi^{-1}(1-\alpha)\big), \qquad \text{AUC} \;=\; \Phi\!\left(\frac{\mu_z}{\sqrt{2}}\right),$$

with Φ the standard normal CDF. Equation (8) is the analytic backbone of the Monte-Carlo study of §3: substituting the frozen window means gives $\text{AUC} = \{0.921, 0.976, 0.992\}$ for {strain, magnetization, fused}, and $\text{TPR}(0.01) = \{0.372, 0.671, 0.857\}$ — exactly the trip-relevant low-false-alarm corner where fusion helps most. The protection decision lives at small α, and the fusion gain in equation (8) is largest there because a shift in μ_z moves TPR fastest on the steep flank of Φ.

IN-WINDING NV SHOT-NOISE SENSITIVITY AND DUAL-MODE READOUT

The magnetization channel is read locally by an ensemble of N_{NV} nitrogen-vacancy centres. The NV ground state is a spin triplet with the Hamiltonian

[redacted]

so that a field along the NV axis Zeeman-splits the $m_s = \pm 1$ sublevels by $2\quad \gamma_{\text{NV}} B_{\parallel}$ (the *field* readout), while temperature and strain shift the zero-field-splitting parameter D (the *mechanical* readout); figure 2 shows the level structure. A single in-winding NV ensemble therefore supplies both the magnetization precursor and a co-located strain check (register item 39). Optically-detected magnetic resonance in the Ramsey mode is shot-noise limited at

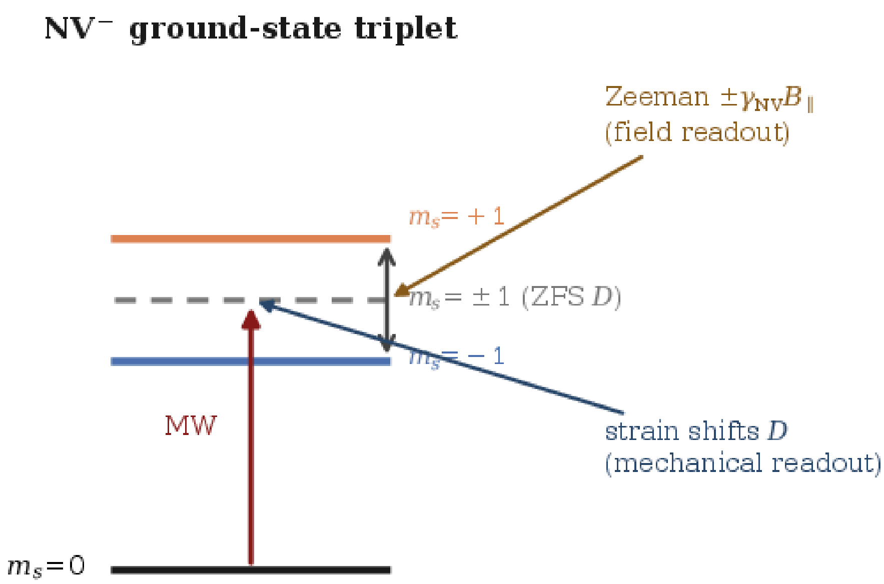

A single in-winding NV ensemble reads local field (Zeeman) and strain (ZFS) simultaneously (KX-L1-A22 / register item 39).

(Schematic.) Dual-mode readout of the in-winding NV ensemble from the ground-state spin Hamiltonian, equation (9). A field along the NV axis Zeeman-splits the $m_s = \pm 1$ sublevels (field readout); temperature and strain shift the zero-field-splitting parameter D (mechanical readout). One ensemble reads both the magnetization precursor and a co-located strain check.

$$\delta B = \frac{1}{\gamma_{\mathrm{NV}}\, C\, \sqrt{N_{\mathrm{NV}}\, T_2^*\, t}},$$

with C the readout figure of merit (contrast × collection efficiency) and T_2^* the ensemble dephasing time. For a conservative in-winding chip ($N_{\mathrm{NV}} = 10^{12}$, $T_2^* = 1\,\mu s$, $C = 0.03$) equation (10) gives $\delta B = 0.189$ pT Hz$^{-1/2}$. A Ramsey shot of $\tau_{\mathrm{shot}} = 4\,\mu s$ (interrogation plus reset) fixes a bandwidth $1/(2\tau_{\mathrm{shot}}) = 125$ Hertz$and a per-shot floor$ B_ shot= BBW $. The full-shed field step of equation$ (???), B\approx100 mT$, then stands

$$\mathrm{SNR}_{\mathrm{shot}} = \frac{\Delta B}{\delta B_{\mathrm{shot}}} \approx 1.5 \times 10^{9}$$

above the per-shot noise, so the precursor is single-shot detectable in one $4\,\mu s$ Ramsey shot; the lead time is set by the millisecond NZPV crossing of equation (2), not by the microsecond sensor latency. The picotesla sensitivity is not *needed* to see a millitesla step — its value is the enormous margin (equation 11) it leaves for multiplexing many in-winding channels and for tolerating in-service degradation of T_2^* and C (§6).

§ 3

Computational methodology

GPU-ACCELERATED MONTE-CARLO ROC SYNTHESIS

The detection metrics are produced by a frozen Monte-Carlo experiment (KX-L1-A20). We draw 2×10^4 null and 2×10^4 fault realisations per class. Each realisation is a detection window of $N = 27$ samples at $f_s = 200$ Hertz(T_w=0.138 s); $the per - sample precursor SNRs are set deliberately low$(SNR_ sample$of$0.35$for strain and$0.5$for magnetization, i.e.$ 10––30× $below the design - basis fault) so that the study lives in the weak - fault regime where a detector's separation is informative, rather than the saturated regime in which every detector scores$ AUC\to1 $. The matched - filter statistic of equation (???) is applied per channel; the fused statistic follows equation (???); the ROC is integrated on a logarithmic false - positive grid and the AUC is estimated by the Mann -- Whitney$ U$identity. The experiment is deterministic under the campaign seed20260825. The Monte - Carlo AUC standard error at$AUC=0.99 andn=2\times10^4is\sigma_ AUC\!\!AUC(1-AUC)/n\!\!7\times10^-4 $, so the reported third decimal is significant; regenerating the ROC from the frozen window means (equation ???) reproduces$ AUC=\0.922,0.976,0.992$ within this error, confirming the closed-form and the Monte-Carlo agree. The vectorised trial ensemble and the accompanying graph-neural-network reconstructor (§4.5) are executed on the NVIDIA GPU HPC campaign.

THE NV ANALYTICAL SENSOR MODEL

The sensor metrics are the analytical evaluation of equations (10)–(11) at the conservative in-winding parameter set (KX-L1-A22), carried in double precision. The model returns $\gamma_{NV} = 28.03$ Hertz, B=0.189 ,BW=125 , $\Delta B = 100\, mT$ at $d = 2\, mm$, and $\mathrm{SNR}_{\mathrm{shot}} = 1.49 \times 10^9$. The sensitivity scaling $\delta B \propto N_{\mathrm{NV}}^{-1/2}$ over four decades of ensemble size (figure 5b) locates the operating point relative to the picotesla-and-below envelope established for ensemble NV magnetometry [11].

FEA-GROUNDED COIL CRITICAL-SURFACE LOAD-LINE

The protective observable of the magnet twin is the current-sharing temperature margin $\Delta T = T_{\mathrm{cs}} - T_{\mathrm{op}}$ along the coil load line (KX-L1-A15). The critical current per tape $I_c(B,T)$ is taken from a fit to the coated-conductor critical surface; at a design tape current $I_{\mathrm{tape}} = 80\, A$ the current-sharing temperature solves $I_{\mathrm{tape}} = I_c(B, T_{\mathrm{cs}})$, and the load fraction is $f_{\mathrm{load}} = I_{\mathrm{tape}}/I_c(B, T_{\mathrm{op}})$. Evaluated on the two distinct magnets' critical surfaces the load line gives, at the design current, a breeder-centrepost margin $\Delta T \approx 49.5\, K$ ($f_{\mathrm{load}} \approx 0.27$, $I_c \approx 293.8\, A$ /tape, $16.84\, T$) and a burner-plug margin $\Delta T \approx 37.1\, K$ ($f_{\mathrm{load}} \approx 0.43$, $I_c \approx 184.3\, A$/tape, $26.49\, T$), with an irreversibility field of $B_{\mathrm{irr}} \approx 102\, T$ at operating temperature. Keeping the two magnets on their own critical surfaces — never conflating the centrepost field with the plug field — is a load-bearing element of the magnet-integrity case; the three-dimensional structural finite-element solve of the $26.49\, T$ plug pack is reported separately [35].

IN-WINDING NEUTRON ENVIRONMENT

The in-winding NV chip sees the centrepost neutron field. Monte-Carlo transport of the $14\, MeV$ source (OpenMC/ENDF-B-VIII.0) [13] sets the centrepost fast-fluence and displacement-damage rate that any in-winding diagnostic must survive; the frozen breeder damage anchor is ~ 19 dpa per full-power year at the first-wall-referenced flux, with the centrepost fluence steeply shielded by the inboard tungsten-carbide budget [30]. The first-principles radiation tolerance of the REBCO tape itself — chain-oxygen-vacancy formation and displacement cascades — is treated in the companion materials study [34]; here it enters only as the requirement that fixes the NV neutron-tolerance gate of §6.

THE NVIDIA GPU HPC CAMPAIGN AND REPRODUCIBILITY

All results were produced within the Kronos de-risking campaign on the NVIDIA GPU HPC fleet (A100/H100/A10 class). For this paper the codes actually run were: the vectorised detection Monte-Carlo and matched-filter/ROC engine of the Kronos toolkit (KX-L1-A20); the double-precision NV sensor model (KX-L1-A22); the FEA-grounded coil critical-surface load-line (KX-L1-A15), with the plug structural solve carried in a 3-D finite-element solver [35]; OpenMC/DAGMC Monte-Carlo neutron transport for the in-winding fluence [13]; and the graph-neural-network state reconstructor (KX-L1-A12) that supplies the model-fusion backup channel of §4.5. Reproducibility is by construction: the deterministic seed is fixed; every headline quantity is one of the frozen anchors verified in the register's reproducibility suite (19/19 anchors reproduced, KX-L1-A6/A10); and the figure-generation script regenerates each data figure from the frozen anchor set. No result depends on unpublished or proprietary data, and no compute-cost figures enter any claim.

§ 4

Results and verification

DETECTION PERFORMANCE

Figure 3 shows the receiver-operating characteristic of the three detectors on a logarithmic false-positive axis that resolves the trip-relevant corner, and figure 3 the same result as an AUC/TPR bar comparison. The fused detector dominates either channel across the full curve: it reaches $\mathrm{AUC} = 0.992$ against 0.976 for magnetization and 0.921 for strain, and at the 1% false-positive rate that a protection trip demands it reaches a true-positive rate of 0.857, versus 0.671 and 0.372 for the single channels; at 0.1% false alarm the gap widens to 0.597 versus 0.386 and 0.135 (table 1). Figure 4 draws the quadrature geometry of equation (7): two window statistics of 2.00 and 2.78 combine to 3.38, and it is this larger mean that sets the fused ROC through equation (8). The fusion of two uncorrelated precursors also suppresses false trips relative to either channel alone, because a coincident excursion in both mechanical and magnetic channels is far rarer than an excursion in either.

CHANNEL	WINDOW MEAN μ_z	AUC	TPR @ 1% FPR	TPR @ 0.1% FPR
fibre-Bragg strain-rate	2.00	0.921	0.372	0.135
magnetization (NV)	2.78	0.976	0.671	0.386
fused (strain-rate + magnetization)	**3.38**	**0.992**	**0.857**	**0.597**

Fused quench-precursor detection (KX-L1-A20; T-synthetic, 2×10^4 trials/class, seed 20260825). The fused detector dominates the full ROC. Window-statistic means $2.00/2.78/3.38$ follow the quadrature rule of equation (7); the AUC and TPR values follow the closed-form ROC of equation (8).

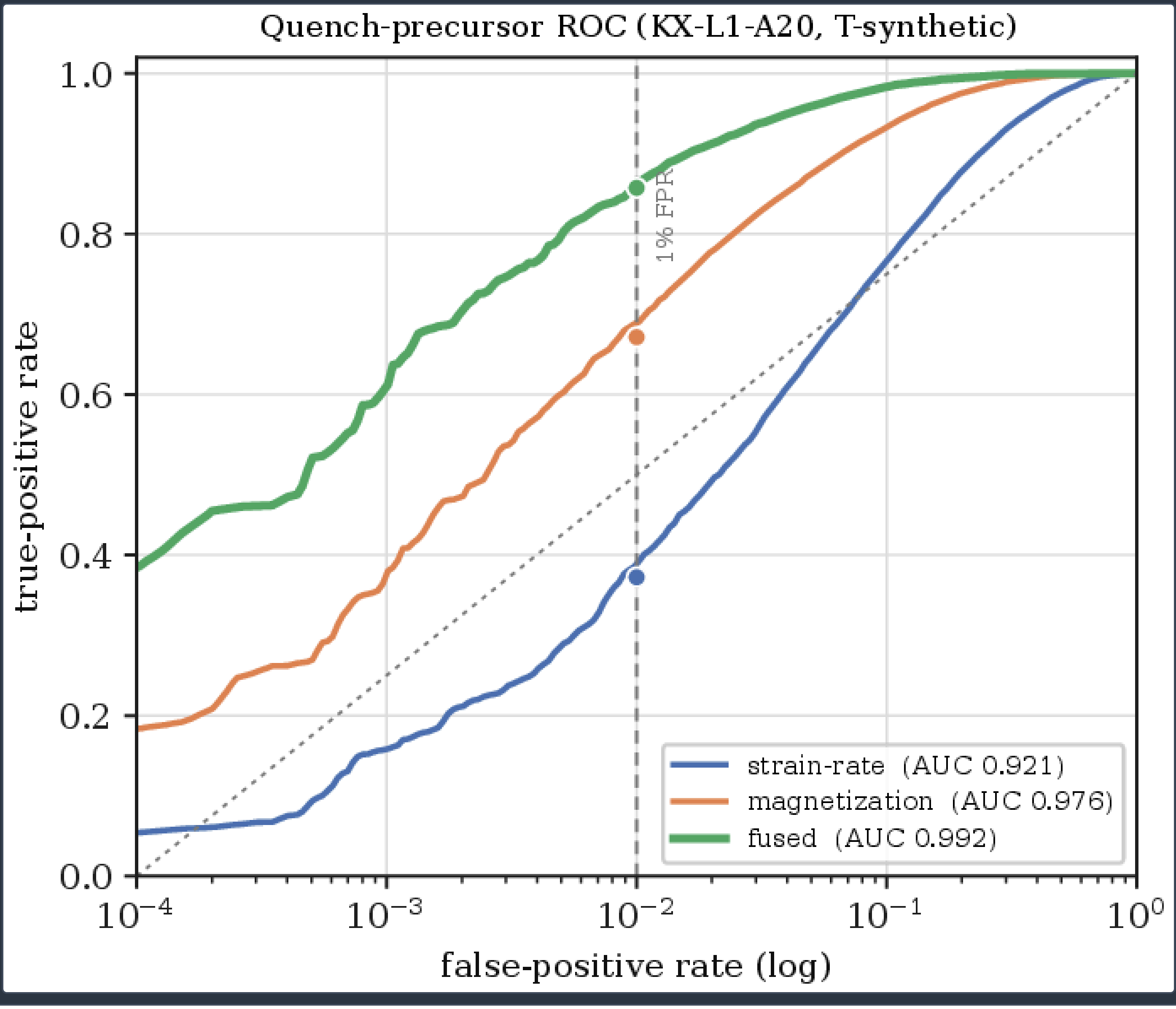
Quench-precursor ROC (KX-L1-A20, T-synthetic)
true-positive rate
false-positive rate (log)
1.0
0.8
0.6
0.4
0.2
0.0
10^{-4}
10^{-3}
10^{-2}
10^{-1}
10^{0}
1% FPR
strain-rate (AUC 0.921)
magnetization (AUC 0.976)
fused (AUC 0.992)

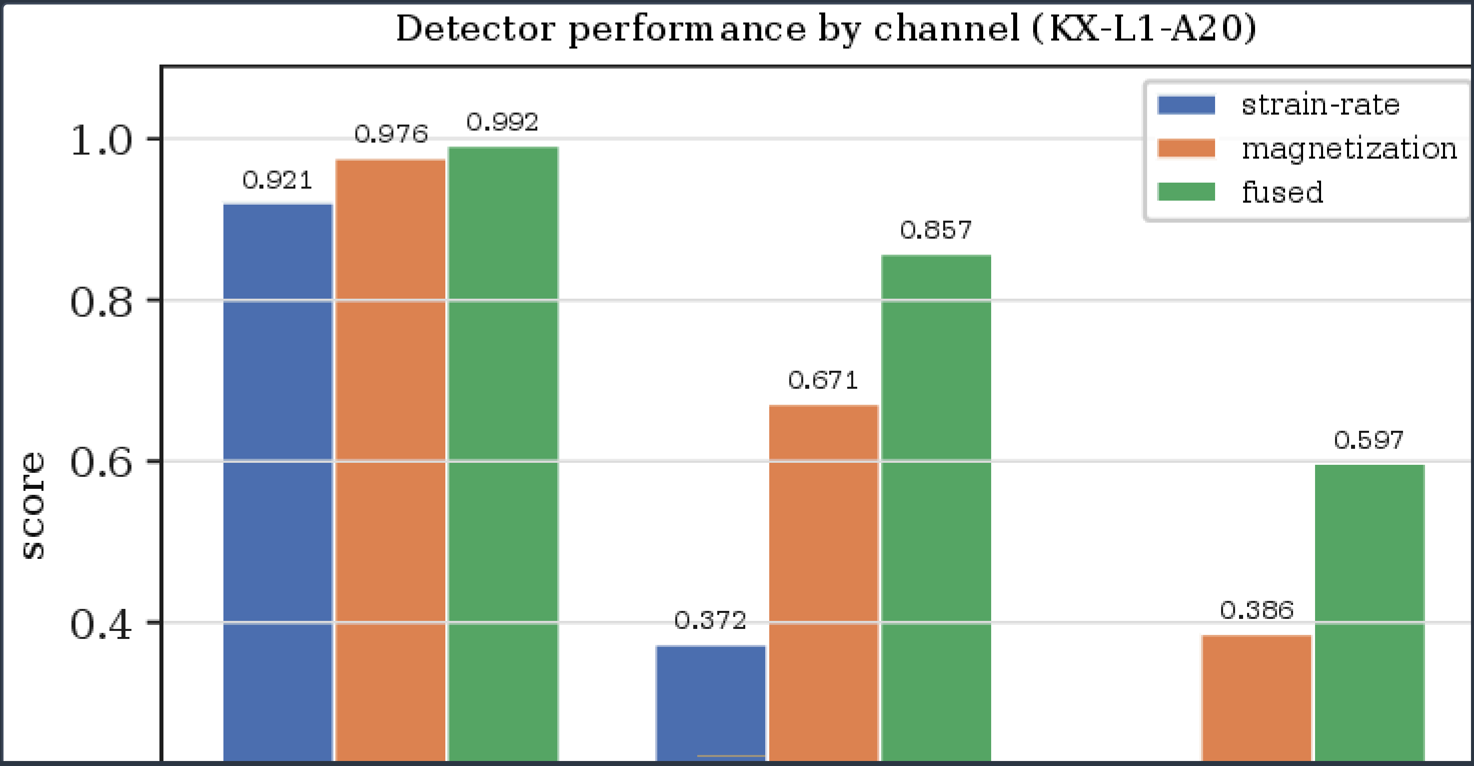
Detector performance by channel (KX-L1-A20)
score
1.0
0.8
0.6
0.4
strain-rate
magnetization
fused
0.921
0.976
0.992
0.372
0.671
0.857
0.386
0.597

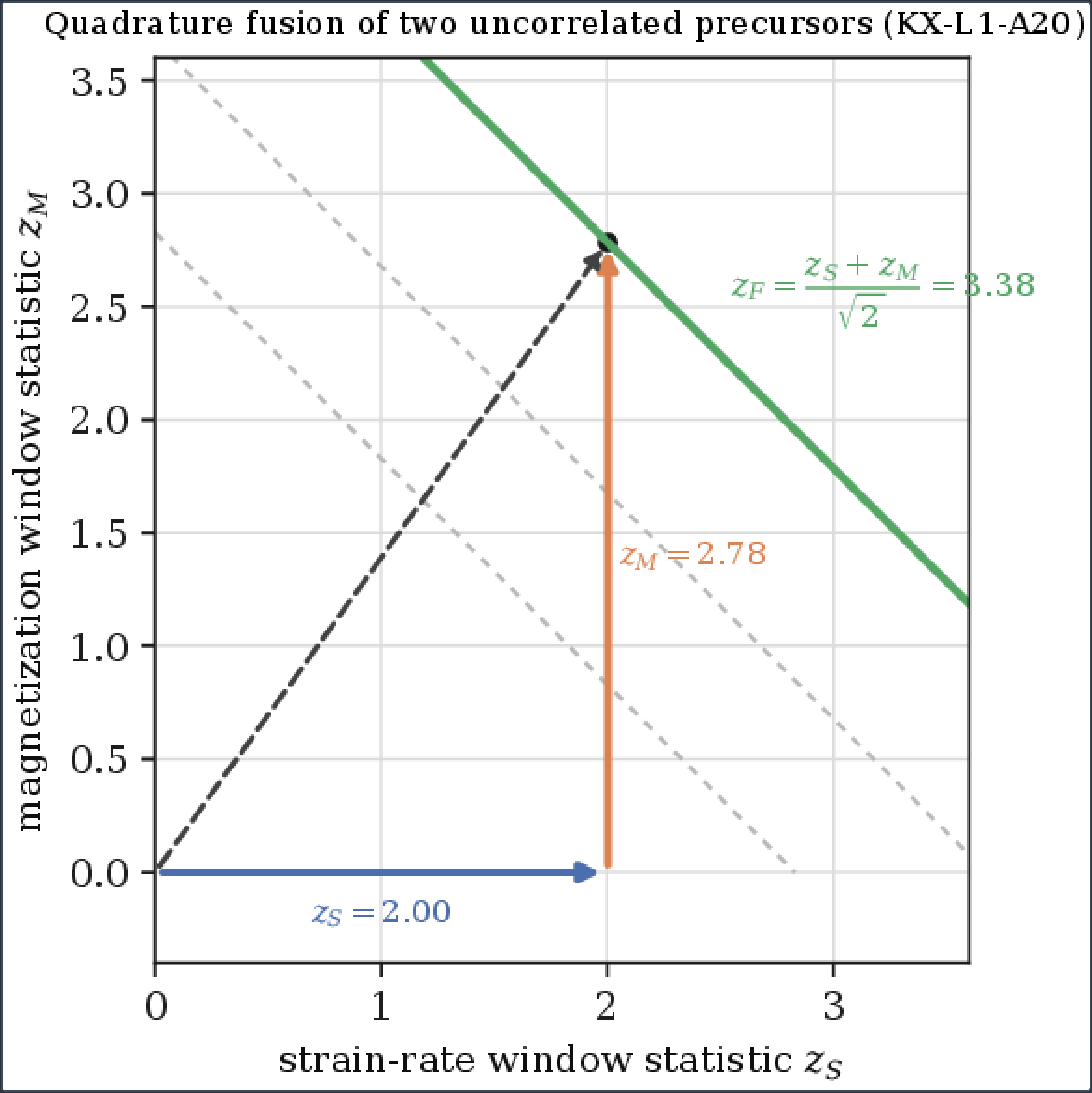

Quadrature fusion of two uncorrelated precursors (KX-L1-A20). The strain-rate and magnetization window statistics $z_S = 2.00$ and $z_M = 2.78$ combine through equation (7) to a fused statistic $z_F = 3.38$; the solid line is the locus of constant fused statistic through the operating point.

THE IN-WINDING NV SENSOR

Figure 5 reports the NV magnetometer (KX-L1-A22). Panel (a) is a signal-versus-noise level diagram: the $100\,mT$ quench field step of equation (5) stands $\sim 10^9$ above the $125\,\mathrm{Hertz} per-shot floor derived from the$ 0.189 $ sensitivity, so equation (11) holds by a vast margin. Panel (b) is the shot-noise sensitivity scaling of equation (10) against ensemble size, with the conservative operating point marked. Table 2 collects the sensor parameters and their basis. The message is one of margin, not of an aggressive device: the parameter set is well inside the reported NV envelope [10,11,12], and the nine-order-of-magnitude per-shot headroom is what the design spends on multiplexing and on tolerating in-service degradation.

QUANTITY	VALUE	BASIS
gyromagnetic ratio γ_{NV}	28.03 $Hertz	NV electron spin, eq. (9)
ensemble / dephasing / readout	$N_{NV} = 10^{12}$, $T_2^* = 1\,\mu s$, $C = 0.03$	conservative in-winding chip
sensitivity δB	0.189 $\mathrm{pT\,Hz^{-1/2}}$	shot-noise limit, eq. (10)
bandwidth	125 $Hertz	4 µs Ramsey shot
quench field step ΔB ($d = 2\,mm$)	$\approx 100\,mT$	full-turn screening shed, eq. (5)
per-shot signal-to-noise ratio	$\sim 1.5 \times 10^9$	eq. (11)
detection	single 4 µs shot	lead set by NZPV (∼ms)

In-winding NV-diamond quench-precursor sensor (KX-L1-A22). Sensitivity and bandwidth from equation (10); the quench step and per-shot SNR from equations (5) and (11).

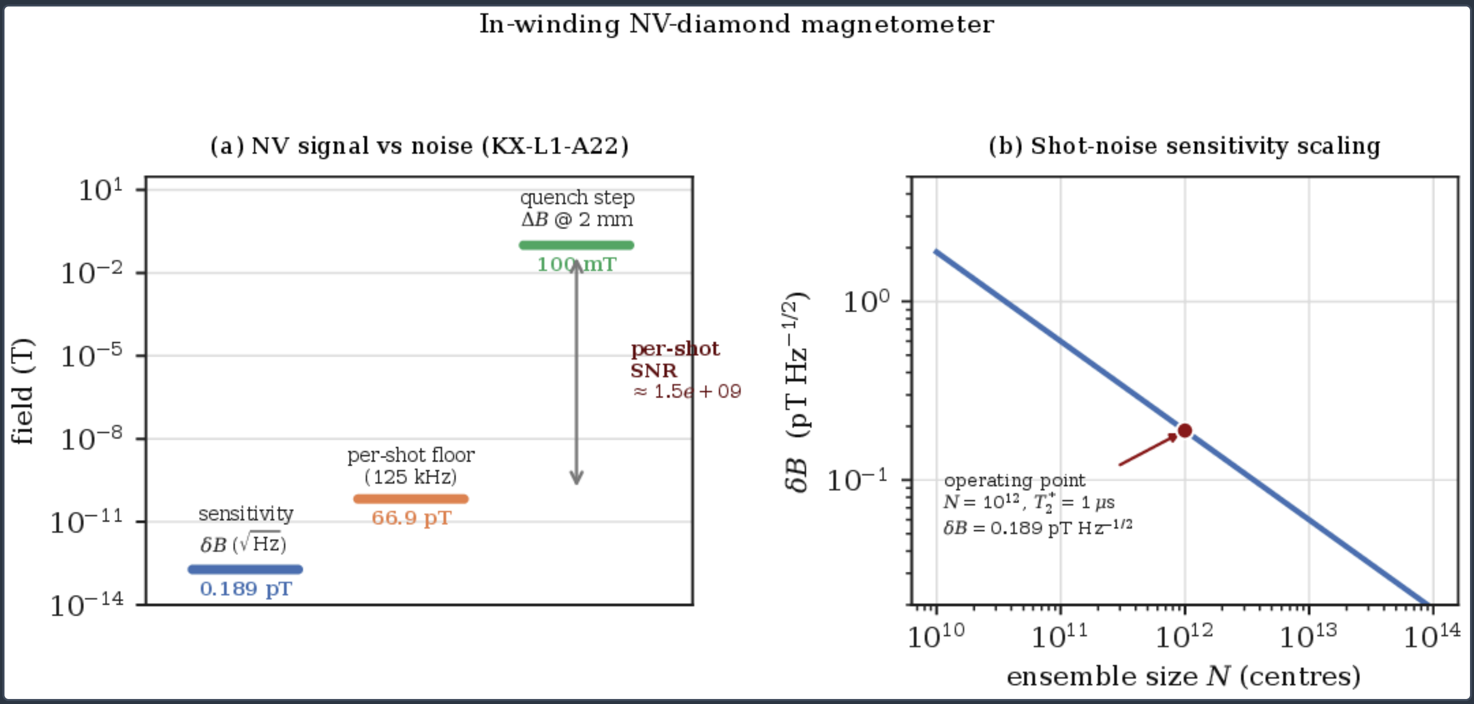

In-winding NV-diamond magnetometer (KX-L1-A22). **(a)** Signal-versus-noise level diagram: the $100\,mT$ quench step stands $\sim 10^9$ above the $125\,\mathrm{Hertz} per-shot floor derived from the$ 0.189 $ sensitivity. **(b)** Shot-noise sensitivity scaling of equation (10) versus ensemble size, with the operating point marked. Panel (b) is a derived scaling curve, not measured data.

THE MIITS LEAD

Figure 6 translates the detection lead into the hot-spot budget of equation (1). The adiabatic peak temperature rises monotonically with the detection-plus-dump delay t_d; a fused precursor that delivers usable warning tens of milliseconds ahead of the terminal-voltage signal keeps the peak temperature back under the conductor limit. Against the register's strong-regime timing anchor (item 36), the fused precursor provides $47.2\,ms$ of usable lead versus $2.6\,ms$ for terminal-voltage detection — an $\sim 18\times$ lead on the fastest magnet-protection channel — which is the reduction in accumulated MIITs that moves the hot spot inside its limit. The curve in figure 6 is a model illustration; the two marked delays are the frozen register warning times.

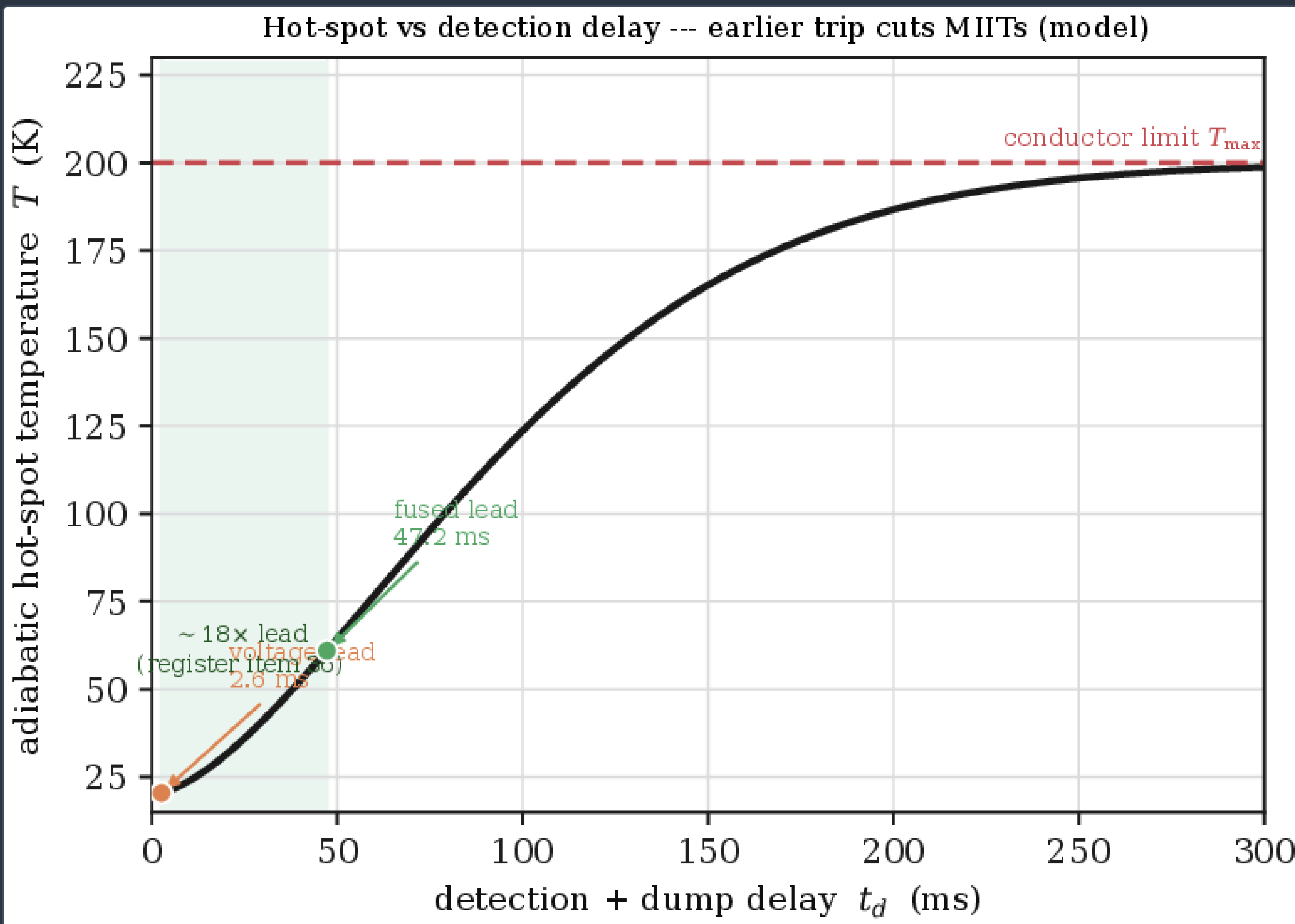

Adiabatic hot-spot temperature versus detection-plus-dump delay from the MIITs integral of equation (1) (model curve). The two marked delays are the frozen register warning times: fused precursor $47.2\,ms$ versus terminal-voltage $2.6\,ms$ (register item 36), an $\sim 18\times$ lead. Earlier tripping keeps the peak temperature below the conductor limit.

TWO DISTINCT MAGNETS

Figure 7 draws the magnet-twin temperature-margin load line for the two distinct magnets (KX-L1-A15). The breeder centrepost governs at a peak field of $16.84\,T$ with a design-current margin $\Delta T \approx 49.5\,K$; the burner plug of the separate burner product is a distinct, higher-field magnet at $26.49\,T$ with $\Delta T \approx 37.1\,K$. The twin's protective observable is the modelled-versus- measured drift of ΔT toward the current-sharing line ($\Delta T \to 0$). Table 3 gives the two critical-surface load points. Treating the centrepost field as an underestimate of the plug field, or vice versa, would corrupt both the quench-margin budget and the sensor placement; the detector models each magnet on its own surface.

MAGNET	PEAK FIELD (T)	I_c/TAPE (A)	f_{load}	ΔT (K)
breeder centrepost	16.84	293.8	0.27	49.5
burner plug (separate product)	26.49	184.3	0.43	37.1

The two distinct magnets on their own critical surfaces (KX-L1-A15). $f_{\text{load}} = I_{\text{tape}}/I_c(B, T_{\text{op}})$ at $I_ tape=§I80

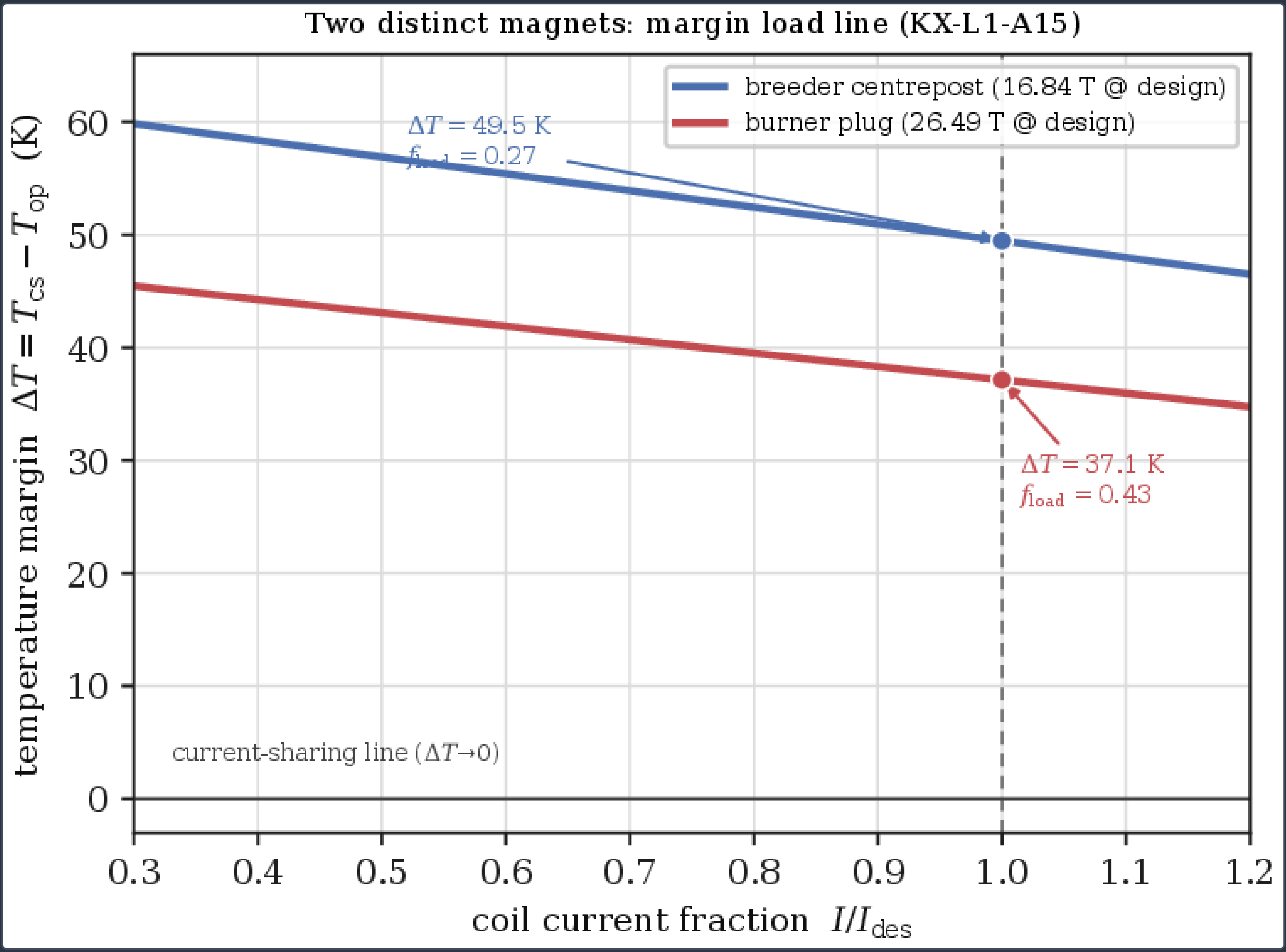

Magnet-twin temperature-margin load line (KX-L1-A15) for the two distinct magnets. Markers show the design current $I/I_{\text{des}} = 1$: breeder centrepost $\Delta T \approx 49.5\,K$ at $16.84\,T$; burner plug $\Delta T \approx 37.1\,K$ at $26.49\,T$.

NEUTRON-DEGRADATION RETENTION

The one open item is the NV sensor's neutron tolerance (§6); its protective consequence is bounded here. Figure 8 shows the precursor AUC under four configurations. With a healthy NV the fused detector holds $\mathrm{AUC} = 0.992$; if the NV (magnetization) channel is lost and only the two-channel quadrature remains, the detector falls back to the strain-only $\mathrm{AUC} = 0.921$. The model-fusion backup (KFE-CF-SH-037) substitutes a graph-neural-network virtual sensor — itself an $\mathrm{AUC} = 0.980$ reconstructor (KX-L1-A12) — so that the protective function is retained at $\mathrm{AUC} \geq 0.95$ even with the NV channel degraded by up to $39\times$. The protective floor therefore survives a heavily degraded sensor; the neutron gate is a sensor-lifetime and sensor-multiplexing question, not a loss-of-protection question.

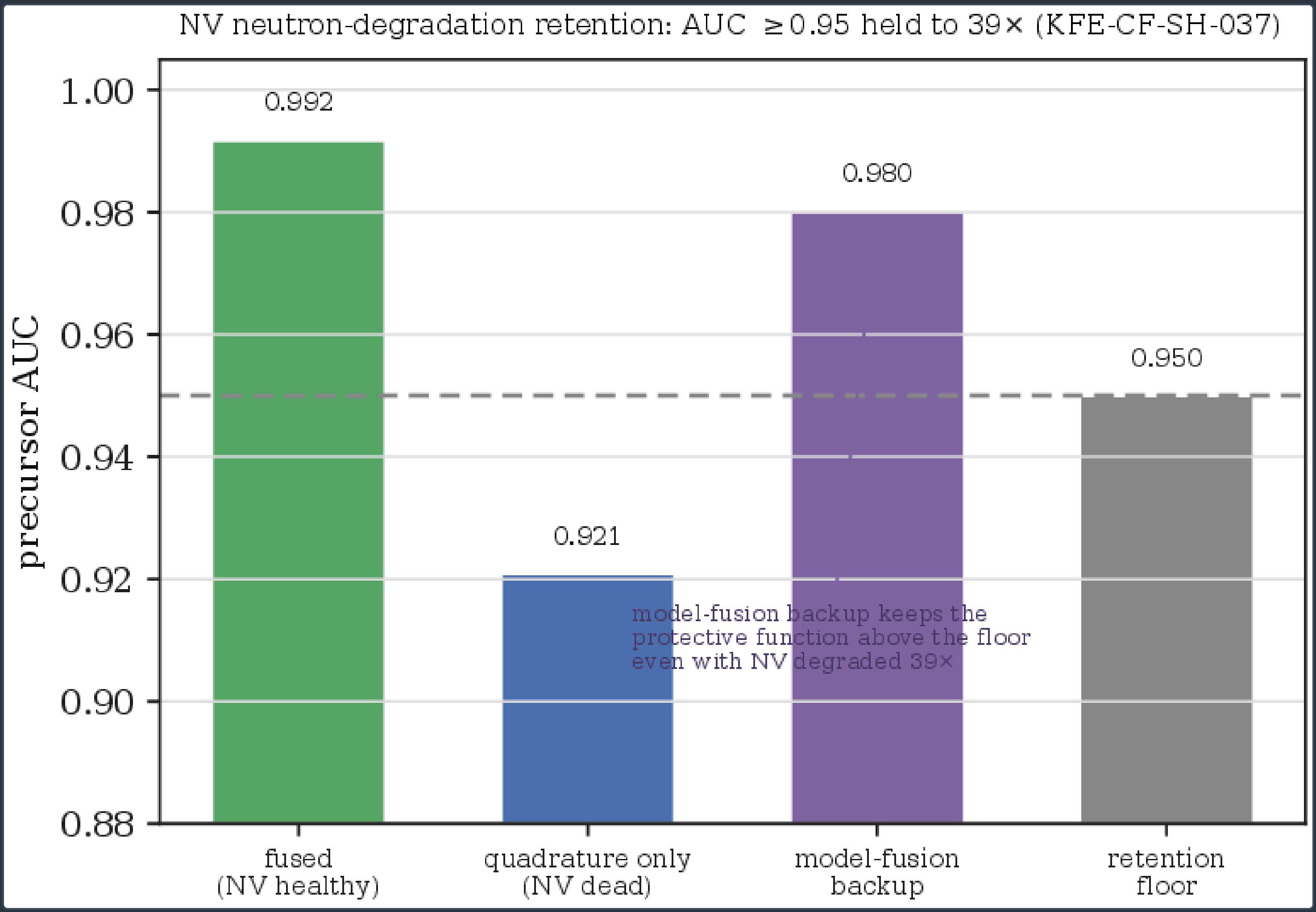

NV neutron-degradation retention (KFE-CF-SH-037). With NV healthy the fused detector holds AUC **0.992**; losing the NV channel entirely drops the two-channel quadrature to the strain-only **0.921**; the model-fusion backup (GNN virtual sensor, KX-L1-A12) holds AUC $\geq$ **0.95** with the NV degraded up to **39**$\times$. Values are frozen roster anchors.

ACCEPTANCE-CRITERIA STATUS

Table 4 collects the demonstrated metrics with their register serials and status. The detection and sensor metrics are demonstrated at twin-synthetic and analytical fidelity; the neutron-tolerance retention is a pre-registered engineering target realised in model fusion; hardware-in-the-loop confirmation on a coil prototype is the gate to a magnet-qualified system (§6).

METRIC	VALUE	SERIAL	STATUS
fused precursor AUC	dominate single channels	KX-L1-A20	demonstrated (0.992)
fused TPR @ 1% FPR	$>$ single channels	KX-L1-A20	demonstrated (0.857)
window-statistic fusion	quadrature rule, eq. (7)	KX-L1-A20	demonstrated (3.38)
NV sensitivity δB	shot-noise limited	KX-L1-A22	analytical (0.189 $\mathrm{pT\,Hz^{-1/2}}$)
NV per-shot SNR	$\gg 1$ for mT step	KX-L1-A22	analytical ($\sim 10^9$)
two-magnet margin map	centrepost / plug separate	KX-L1-A15	demonstrated (49.5 / 37.1 K)
NV-degradation retention	AUC ≥ 0.95 at $39\times$	KFE-CF-SH-037	target (model fusion)
HIL confirmation	coil-prototype bench	—	open (see §6)

Demonstrated detection/sensor metrics, register serials and status. “Demonstrated (T-synthetic)” denotes a frozen synthetic result; “analytical” denotes a closed-form model evaluation; “target” denotes a pre-registered bar. Serials refer to the register [30].

§ 5

Discussion

QUENCH DETECTION IN CONTEXT

The fused detector should be read against the published quench-detection literature and specifically against the slow-NZPV problem that motivates it. Marchevsky's review makes the core point quantitatively: in HTS conductors the large temperature margin and slow propagation mean a hot spot can reach a damaging temperature before a measurable resistive voltage appears, so voltage detection alone is inadequate [7]. The community response has been non-voltage observables: Salazar *et al.* demonstrated FBG and ultra-long-FBG thermometry on VIPER cable at SULTAN, reporting signal-to-noise ratios of 4–32 for heater-induced quench-like events with response times from effectively instantaneous to a few seconds [8], and Teyber *et al.* showed that current-distribution monitoring detects quench and damage in fusion cables [9]. Our result is complementary and, by construction, evaluated in a harder regime. The ROC of table 1 is computed with per-sample SNRs set 10–$30\times$ below the design-basis fault, precisely to avoid the saturated corner where every detector scores $\mathrm{AUC} = 1$; in that weak-fault regime the fusion of an uncorrelated strain-rate and magnetization pair lifts the true-positive rate at 1% false alarm from $0.372/0.671$ (single channels) to 0.857. For comparison, in the strong-signal regime the same fused architecture scores $\mathrm{AUC} = 0.9998$ with $47.2\,ms$ of usable lead against $2.6\,ms$ for terminal voltage (register item 36) — the saturated benchmark whose number is uninformative about detector *ranking*, which is exactly why the primary result is reported in the weak-fault regime. The message is not that a single AUC beats a single published number, but that channel fusion recovers early, low-false-alarm warning in the low-signal corner that the slow-NZPV physics forces a real magnet into.

NV SENSITIVITY AGAINST THE QUANTUM-SENSING LITERATURE

The in-winding sensitivity of 0.189 $\mathrm{pT\,Hz^{-1/2}}$ sits comfortably inside the envelope established for ensemble NV magnetometry. Degen, Reinhard and Cappellaro's review frames the shot-noise scaling that equation (10) instantiates [10], and Barry *et al.* analyse the concrete route to broadband ensemble sensitivities in the picotesla-and-below range through improvements to T_2^*, readout fidelity and diamond material [11,12]. Our conservative parameter set ($N_{\mathrm{NV}} = 10^{12}$, $T_2^* = 1\,\mu\,s$, $C = 0.03$) is well within what that literature reports, so the sensitivity claim does not rest on an aggressive device. The physically important observation is one of margin: a millitesla quench step is $\sim 10^9$ above the per-shot floor, so the precursor is single-shot detectable and the picotesla headroom is available both for multiplexing many in-winding channels and for tolerating in-service degradation of T_2^* and C. The dual-mode readout of equation (9) — field through the Zeeman splitting and strain through the zero-field-splitting parameter — lets a single ensemble corroborate the magnetization precursor with a co-located strain check, and points toward the entanglement-enhanced magnetometry that the burner quantum stack pursues [37].

WHY FUSION, AND WHY LOCAL

Two design choices carry the result. First, fusion: two prompt precursors that fail in uncorrelated ways combine in quadrature (equation 7), and the closed-form ROC (equation 8) shows the gain is largest at low false-alarm rate — the only regime a protection trip cares about. Second, locality: reading the magnetization channel *inside* the winding with an NV ensemble means the sensor sees the local field step of equation (5) directly, at a standoff of millimetres, rather than a terminal signal averaged over the coil. Locality is what converts the slow-NZPV liability into an asset: the precursor is set by local current redistribution, which is prompt, not by the normal length, which is slow. The architecture is the reduced-to-practice magnet-protection exemplar of the four-twin control stack [31], and it feeds the consumable-centrepost integrity and remaining-life case [32] that schedules cartridge replacement.

§ 6

Limitations

Two honest caveats bound the claims. First, the detection metrics are twin-synthetic: every signal in the ROC study is numerically generated under the model of §2, and the confirming measurement is a coil-prototype hardware-in-the-loop bench, which is the gate to a magnet-qualified protection system. Second — the one open engineering item — the in-winding NV sensor's neutron tolerance: the analytical sensitivity of equation (10) assumes an ensemble T_2^* and contrast C that will degrade under the high background field, cryogenic operation and neutron irradiation of the diamond (NV charge-state stability). The mitigation is threefold and is itself a registered work item (KFE-CF-SH-037): shielded siting, a replaceable sensor cartridge matched to the consumable-centrepost swap cadence, and the model-fusion backup of §4.5 that retains precursor $\mathrm{AUC} \geq 0.95$ with the NV channel degraded by up to $39\times$ — so the protective function survives even a heavily degraded sensor. A dedicated NV neutron-tolerance study (irradiation plus first-principles charge-state modelling, alongside the REBCO tape tolerance work [34]) is the follow-on that closes this item. Nothing here is claimed as a qualified hardware protection system.

§ 7

Conclusion

No-insulation REBCO fusion magnets quench too slowly for terminal-voltage protection, and the resulting hot-spot liability is set by the MIITs integral of equation (1). Fused strain-rate and magnetization sensing does not wait for voltage: two prompt, uncorrelated precursors — the thermal strain rate of equation (4) and the screening-current-decay field step of equation (5) — are reduced to matched-filter window statistics and combined in quadrature (equation 7), giving a detector at $\mathrm{AUC} = 0.992$ and true-positive rate 0.857 at 1% false alarm in a deliberately hard weak-fault regime, dominating either channel alone. The magnetization channel is read locally by an in-winding NV-diamond ensemble at $0.189 \quad \mathrm{pT\,Hz}^{-1/2}$ and a per-shot signal-to-noise ratio of order 10^9 for the conductor-scale field step, with the same ensemble reading field and strain through the NV spin Hamiltonian. Tripping tens of milliseconds early — $47.2\,ms$ against $2.6\,ms$ for voltage — cuts the accumulated MIITs and moves the hot spot inside its limit. The breeder centrepost ($16.84\,T$) and the burner plug ($26.49\,T$) are modelled as the two distinct magnets they are, and the one open item, the NV sensor's neutron tolerance, is bounded by a model-fusion backup that keeps the protective function above an $\mathrm{AUC} = 0.95$ floor at $39\times$ degradation. It is a protection architecture at the model-and-bench stage, stated as such, with a defined and testable path to a magnet-qualified system.

Acknowledgments tocsectionAcknowledgments Part of the Kronos Fusion Energy 2026 design series. The authors thank the Kronos physics de-risking programme for the frozen result set underlying every quantitative claim, and R J Weggel and C Weggel for the magnet and structural basis of the two distinct coils.

Reproducibility. Every headline quantity in this paper is a frozen anchor in the Kronos Physics De-Risking Register [30] (doi:10.5281/zenodo.22133057): the fused-detector ROC (KX-L1-A20), the in-winding NV sensor model (KX-L1-A22), the two-magnet margin load line (KX-L1-A15), the GNN backup channel (KX-L1-A12), and the neutron-degradation retention (KFE-CF-SH-037). Each is regenerable from the archived simulator and the figure-generation script deposited with this paper; this paper is archived at doi:10.5281/zenodo.22645752; official version: https://www.kronosfusionenergy.com/publications/quench-detection-and-nv-sensing.html. No result depends on unpublished or proprietary data, and no economic content is part of the deposit.

Data availability tocsectionData availability The ROC curves, the NV sensor parameters, the coil load-line map, and the retention values used for figures 3–8 are archived with the deposit at doi:10.5281/zenodo.22645752 and trace to the register [30] by the serial identifiers cited inline. The figure-generation script (`make_figs_2–19_quench_nv.py`) regenerates every data figure from the frozen anchors. Any economic analysis is reported separately and is not part of the public deposit.

Competing interests tocsectionCompeting interests Provisional patent applications relating to aspects of this work have been filed.

tocsectionReferences

Portfolio, People & Record

The intellectual-property estate, the people who built it, the limitations that gate it, and the sources it rests on.

1	4	40	27
GRANTED PATENT	2026 PROVISIONALS	TEAM MEMBERS	2022 PROVISIONALS

INTELLECTUAL PROPERTY

The patent portfolio

The estate spans a granted high-field magnet patent, pending utility and 2026 provisional filings that map to the two products, a digital-twin control provisional, a registered trademark application, and the original 2022 provisional family. Every patentable disclosure in the five-paper arXiv drop was protected **before** publication: the breeder and burner provisionals were filed 1–2 August, and a publication-gap omnibus filing the evening before the drop swept up the DEC, plasma-control, and REBCO-winding matter of the three otherwise-unprotected papers. Patent numbers and application serials are matters of public record; claim scope is summarised, not reproduced.

GRANTED & PENDING UTILITY

US 12,009,112	High-field tilted graded-REBCO magnet architecture (KRONO-002A) · *app. 17/878,550*	GRANTED
US 17/878,507	Core device / method (KRONO-001A) · *utility*	PENDING

2026 PROVISIONAL FILINGS — MAPPED TO THE PRODUCTS

64/124,209	Hyperion — spherical-tokamak tritium / helium-3 foundry · *breeder · filed Aug 2026*	FILED
64/124,220	Aegis / MetroVolt — synchrotron-cutoff, fuel-selection & plug-winding · *generator · filed Aug 2026*	FILED
64/115,167	KRONOS-CTRL digital-twin plant control · *provisional · filed Jul 2026*	FILED
64/005,440	Integrated spherical-tokamak fusion architecture · *early integrated-architecture filing · filed Mar 2026*	FILED
64/105,530	Negative-triangularity spherical-tokamak architecture · *foundational ST filing · filed Jul 2026*	FILED
64/128,097	Publication-gap omnibus — quasineutral two-species expander DEC · provenance-gated / latency-split plasma control · as-built high-field winding & conductor architecture · *filed 7 Aug 2026, the evening before the arXiv drop*	FILED

TRADEMARK & ORIGIN

FTK-98801894	Kronos Fusion Energy — trademark application	FILED
KR-2022-*	Original provisional family (KR-2022-00001 … 00027) · *27 filings, 2022*	PRIORITY

The narrow, defensible magnet novelty — the specific conductor and the digital-twin winding optimisation, not high-field REBCO as a category — is the commercial core that can earn ahead of any Q > 1 milestone, with markets in fusion magnet supply, MRI/NMR, accelerators, and proton therapy. The claim is scoped honestly: the high field is a *system field* result, not a stand-alone-coil record; the small-bore plug coil is structurally infeasible as a bare winding but resolved by a stress-managed structural shield (feasible-pending-FEA); and the winding-tape experiment returned a *null result*. The value is the method, not a field record.

THE TEAM

Founding partners, board, advisors & auditors

Kronos is built by a bench of advanced-fuel-fusion, high-field-magnet, direct-conversion, and materials specialists, with a board and operations team drawn from defense, national laboratories, and industry. Dates are shown as ranges; where a tenure has ended or is term-ending, the range says so.

FOUNDING PARTNERS — SCIENCE

Dr. Gerald Kulcinski
Co-Founder · Helium-3 & Advanced-Fuel Fusion
UW–Madison · 2023–Present

Dr. Carl Weggel
Chief Scientist / S.M.A.R.T. Design
MIT Alcator Program · 2022–Present

Dr. Robert J. Weggel
Magnetic Field Design
MIT Magnet Lab · 2022–Present

BOARD

Priyanca Ford
Founder & CEO · Executive Board
2022–Present

Bandel Carano
Finance / Strategy
Oak Investment Partners / Stanford · 2025–2026

Patrick Schweiger
Fusion Device Engineering
Oklo / CFS / TerraPower · 2025–Present

SCIENTIFIC ADVISORS

Dr. Steven O. Dean
Fusion Policy & History
DOE / Fusion Power Associates · 2025–Present

Dr. Patrick H. Diamond
Plasma Turbulence & Transport
UC San Diego · 2025–Present

Dr. Jack J. Dongarra
HPC & Numerical Algorithms
Turing Award · 2025–Present

Dr. Nasr M. Ghoniem
Chief Material Scientist
UCLA · 2025–Present

Dr. Siegfried Glenzer
Plasma Physics & Laser Fusion
Stanford / SLAC · 2022–Present

Dr. David A. Hammer
Pulsed-Power Fusion
Cornell · 2025–Present

Dr. Donald A. Spong
Plasma Theory & Confinement
ORNL · 2025–Present

Dr. Curtis Smith
Risk Assessment & Nuclear PRA
MIT / Idaho National Lab · 2025–Present

RADM (Ret.) David Goggins
Naval Engineering & Power-Plant Design
U.S. Navy · 2023–2026

Dr. Konstantin Batygin
Mathematician
Caltech · 2022–2025

Dr. Ruben Fair
Magnet Design / ITER Liaison
PPPL / Jefferson Lab · 2022–2025

Dr. Paul S. Weiss
Materials & Nanotechnology
UCLA · 2022–2025

SCIENTIFIC AUDITORS

Dr. Wilfred A. Cooper
Plasma Equilibrium Theory
EPFL / Swiss Plasma Center · 2025–Present

Dr. Ahmed Hassanein
Plasma–Material Interactions
Purdue / Argonne · 2025–Present

Dr. Patrick E. Hopkins
Extreme Thermal Materials
U. of Virginia · 2025–Present

Dr. Peter Hosemann
Materials Joining & Structural Integrity
UC Berkeley · 2025–Present

Dr. Travis W. Knight
Advanced Nuclear Fuels & Systems
U. of South Carolina · 2025–Present

Dr. Philippe Lebrun
Cryogenics & Magnet Cooling
CERN · 2025–Present

Dr. Nitendra Singh
Nuclear Safety & Fuel Cycle
ITER · 2025–Present

Dr. Guido Van Oost
Magnetic Confinement & Fusion Systems
Ghent University · 2025–Present

Dr. Gary S. Was
Radiation Materials & Structural Integrity
U. of Michigan · 2025–Present

Dr. Ray Sedwick
Direct Energy Conversion
U. of Maryland · 2025

OPERATIONS

Michael Laughlin
Chief Operating Officer
2022–Present

Martin Owens
Chief Strategy Officer
LANL / GE Hitachi · 2022–Present

MG (Ret.) Paul Pardew
Chief Contracting Officer
Army Contracting Command · 2022–Present

David Beck
Fusion Commercialization
U.S. Space Force · 2024–Present

Sushma Bhatia
Environmental & Legislative
Google · 2022–Present

Michael De Frenza
Technology Licensing
2023–Present

MG (Ret.) Robin L. Fontes
Cybersecurity & Defense
Army Cyber Command · 2022–Present

Vijay Gehani
Supply Chain & Components
INOX India · 2024–Present

Jon Michel Greenwood
IT & AI Infrastructure
Live Nation · 2023–Present

Brian C. O'Neill
National Security
CIA / ODNI · 2022–Present

Gen. (Ret.) Gustave F. Perna
DoD Liaison
Operation Warp Speed · 2022–2023

Andrea Romero
Marketing Lead
2022–Present

Legal counsel is retained; those roles are held on the internal roster and are not listed here.

SOURCES

References

1 J E Menard *et al*, Fusion nuclear science facilities and pilot plants based on the spherical tokamak, *Nucl. Fusion* **56** 106023 (2016). doi:10.1088/0029-5515/56/10/106023

2 B N Sorbom *et al*, ARC: a compact, high-field, fusion nuclear science facility and demonstration power plant with demountable magnets, *Fusion Eng. Des.* **100** 378 (2015). doi:10.1016/j.fusengdes.2015.07.008

3 A J Creely *et al*, Overview of the SPARC tokamak, *J. Plasma Phys.* **86** 865860502 (2020). doi:10.1017/S0022377820001257

4 S Hahn, Y Kim, D K Park, K Kim, J P Voccio, J Bascu\ n\'an and Y Iwasa, No-insulation multi-width winding technique for high temperature superconducting magnet, *Appl. Phys. Lett.* **103** 173511 (2013). doi:10.1063/1.4826217

5 S Hahn *et al*, 45.5-tesla direct-current magnetic field generated with a high-temperature superconducting magnet, *Nature* **570** 496 (2019). doi:10.1038/s41586-019-1293-1

6 J L MacManus-Driscoll and S C Wimbush, Processing and application of high-temperature superconducting coated conductors, *Nat. Rev. Mater.* **6** 587 (2021). doi:10.1038/s41578-021-00290-3

7 M Marchevsky, Quench detection and protection for high-temperature superconductor accelerator magnets, *Instruments* **5** 27 (2021). doi:10.3390/instruments5030027

8 E E Salazar *et al*, Fiber optic quench detection for large-scale HTS magnets demonstrated on VIPER cable during high-fidelity testing at the SULTAN facility, *Supercond. Sci. Technol.* **34** 035027 (2021). doi:10.1088/1361-6668/abdba8

9 R Teyber, J Weiss, M Marchevsky, S Prestemon and D van der Laan, Current distribution monitoring enables quench and damage detection in superconducting fusion magnets, *Sci. Rep.* **12** 22503 (2022). doi:10.1038/s41598-022-26592-2

10 C L Degen, F Reinhard and P Cappellaro, Quantum sensing, *Rev. Mod. Phys.* **89** 035002 (2017). doi:10.1103/RevModPhys.89.035002

11 J F Barry, J M Schloss, E Bauch, M J Turner, C A Hart, L M Pham and R L Walsworth, Sensitivity optimization for NV-diamond magnetometry, *Rev. Mod. Phys.* **92** 015004 (2020). doi:10.1103/RevModPhys.92.015004

12 L Rondin, J-P Tetienne, T Hingant, J-F Roch, P Maletinsky and V Jacques, Magnetometry with nitrogen-vacancy defects in diamond, *Rep. Prog. Phys.* **77** 056503 (2014). doi:10.1088/0034-4885/77/5/056503

13 P K Romano, N E Horelik, B R Herman, A G Nelson, B Forget and K Smith, OpenMC: a state-of-the-art Monte Carlo code for research and development, *Ann. Nucl. Energy* **82** 90 (2015). doi:10.1016/j.anucene.2014.07.048

14 J Kates-Harbeck, A Svyatkovskiy and W Tang, Predicting disruptive instabilities in controlled fusion plasmas through deep learning, *Nature* **568** 526 (2019). doi:10.1038/s41586-019-1116-4

15 J Degrave *et al*, Magnetic control of tokamak plasmas through deep reinforcement learning, *Nature* **602** 414 (2022). doi:10.1038/s41586-021-04301-9

16 M G Kapteyn, J V R Pretorius and K E Willcox, A probabilistic graphical model foundation for enabling predictive digital twins at scale, *Nat. Comput. Sci.* **1** 337 (2021). doi:10.1038/s43588-021-00069-0

17 L Lu, P Jin, G Pang, Z Zhang and G E Karniadakis, Learning nonlinear operators via DeepONet based on the universal approximation theorem of operators, *Nat. Mach. Intell.* **3** 218 (2021). doi:10.1038/s42256-021-00302-5

18 Z Li, N Kovachki, K Azizzadenesheli, B Liu, K Bhattacharya, A Stuart and A Anandkumar, Fourier neural operator for parametric partial differential equations, *Int. Conf. on Learning Representations (ICLR)* (2021). arXiv:2010.08895

19 M Raissi, P Perdikaris and G E Karniadakis, Physics-informed neural networks: a deep learning framework for solving forward and inverse problems involving nonlinear partial differential equations, *J. Comput. Phys.* **378** 686 (2019). doi:10.1016/j.jcp.2018.10.045

20 K L van de Plassche, J Citrin, C Bourdelle *et al*, Fast modeling of turbulent transport in fusion plasmas using neural networks, *Phys. Plasmas* **27** 022310 (2020). doi:10.1063/1.5134126

21 R E Kalman, A new approach to linear filtering and prediction problems, *J. Basic Eng.* **82** 35 (1960). doi:10.1115/1.3662552

22 G Evensen, The ensemble Kalman filter: theoretical formulation and practical implementation, *Ocean Dyn.* **53** 343 (2003).

COLOPHON

How this document was made

The Kronos Fleet — Combined Editorial, 2026 is set in **Fraunces** (display), **Gelasio** (text), and **IBM Plex Mono** (data & equations), carried forward from the Kronos editorial design system.

The figures are rendered at 300 dpi from the deposited generator scripts; the document is composed as a single self-contained file with embedded fonts and imagery, paginated to US Letter, and rendered to PDF through a headless Chromium engine in matched light and dark editions.

Every headline quantity carries an evidence class; withdrawn and restated values are marked as such. Nothing herein is frozen beyond the founder-approved Tier-A set.

Explore it live — turn the interactive 3-D model, run the deposited solvers in the physics validator, and watch the companion film series.

LEGAL NOTICE

Notice, status, and distribution

Conceptual design & simulation study. This document reports a conceptual design and simulation study. It is not a construction commitment, a safety-analysis report, a regulatory filing, or an offer of securities. Forward-looking statements — schedules, costs, market sizes, and performance — are estimates subject to the limitations set out in the Simulations part and may change.

Numbers and their classes. Quantities are reported with evidence classes and case labels; modelled, assumed, and requirement-class values are identified as such and are not to be quoted without their labels.

Public edition. This edition carries the physics and design only; all financial, funding, and defense-commercial content has been removed for public distribution. The scientific text corresponds to the arXiv and journal submissions.

THE 2026 KRONOS SERIES

One programme, many papers

This editorial is one paper in the Kronos 2026 series — a real fusion company's complete, reproducible physics record for a spherical-tokamak breeder and its low-neutron D–^{3}He tandem-mirror burners. Every headline number is a frozen anchor in the Physics De-Risking Register.

Explore the whole programme: the De-Risking Register, the interactive 3-D model, and the physics validator.

KRONOS FUSION ENERGY

Fused Strain-Rate and Magnetization Quench Detection with In-Winding NV-Diamond Sensing for No-Insulation REBCO Breeder Magnets

A real fusion company building real machines. Explore the science, live.

Zenodo · doi:10.5281/zenodo.22645752

Read on kronosfusionenergy.com

The Physics De-Risking Register